

2D+3D Facial Expression Recognition via Discriminative Dynamic Range Enhancement and Multi-Scale Learning

Yang Jiao^{†,‡}, Yi Niu[†], Trac D. Tran[‡], Guangming Shi[†]
[†] Xidian University, [‡] Johns Hopkins University

Abstract

In 2D+3D facial expression recognition (FER), existing methods generate multi-view geometry maps to enhance the depth feature representation. However, this may introduce false estimations due to local plane fitting from incomplete point clouds. In this paper, we propose a novel Map Generation technique from the viewpoint of information theory, to boost the slight 3D expression differences from strong personality variations. First, we examine the HDR depth data to extract the discriminative dynamic range r_{dis} , and maximize the entropy of r_{dis} to a global optimum. Then, to prevent the large deformation caused by over-enhancement, we introduce a depth distortion constraint and reduce the complexity from $O(KN^2)$ to $O(KN\tau)$. Furthermore, the constrained optimization is modeled as a K -edges maximum weight path problem in a directed acyclic graph, and we solve it efficiently via dynamic programming. Finally, we also design an efficient Facial Attention structure to automatically locate subtle discriminative facial parts for multi-scale learning, and train it with a proposed loss function \mathcal{L}_{FA} without any facial landmarks. Experimental results on different datasets show that the proposed method is effective and outperforms the state-of-the-art 2D+3D FER methods in both FER accuracy and the output entropy of the generated maps.

1. Introduction

Facial expression – the most primary and straightforward nonverbal way to convey the emotion of a human being – plays an essential role not only in human-behavior analysis [10, 20] but also in human-machine interaction [24, 19, 4]. In recent years, 3D and 2D+3D based Facial Expression Recognition (FER) have attracted much attention to overcome non-ideal lighting conditions and large pose variations from RGB data, since the depth and texture are somewhat complementary for expression representation.

However, even with the aid of 3D information, multi-modality FER is still challenging since facial features are

dominated by strong personality (intra-class) differences, but not by slight expression (inter-class) variations. For example, muscle movements from Angry to Sadness only cause minor inter-class differences because of the invariance of facial structure. However, diversity of independent subjects (e.g., gender, age, race) introduces large intra-class variations to expression data. Therefore, enhancing weak expression features from strong personality variations is the key for successfully recognition. To this end, *Map Generation* has been designed as a critical and indispensable stage in the 2D+3D FER pipeline, where raw 3D scans are comprehensively represented by a series of attribute maps.

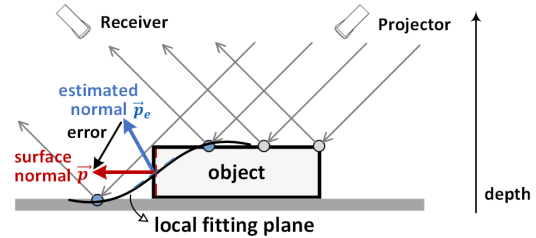


Figure 1. False normals are introduced by local plane fitting.

Problem. In the current literature [31, 13, 34, 30, 16, 29, 35, 5], geometrical information is widely explored to describe raw 3D scans for map generation. For instance, Yang *et al.* [30] generates curvature maps (CuM) from 3D face model to enhance the facial landmarks, and Zhen *et al.* [34] extracts normal maps (NoM) and shape index maps (SIM) values to describe the geometry deformation of facial regions. Recently, diverse geometry maps (GeM) are combined together to further promote the feature learning in deep neural networks as adopted in [16, 3, 35]. These methods provide elegant directions to enhance 3D expression features from multi-geometry views. However, considering that in real FER applications, depth data are only acquired once from the view of frontal face. This one-shot setup can only sample an incomplete 3D data of the scene, missing the point clouds that might be essential for geometry estimation. In other words, the generated multi-view geometry maps in existing methods are NOT projected by the

real 3D objects, but estimated by local plane fitting [8, 6]. Unfortunately, fitting a surface plane with incomplete data may bring false geometrical attributes to the generated map as illustrated in Fig. 1, and decreases recognition performances. In the figure, the estimated normal \vec{p}_e (blue arrow) from local fitting plane introduces the error (black arrow) to the real surface normal \vec{p} (red arrow).

Motivation. Taking a different approach from current works, we are inspired by the fact that depth scans are sampled by high dynamic range (HDR) point clouds, while inter-class differences are only represented by a limited dynamic range, indicating a low signal-to-noise ratio (SNR) of raw 3D expression scans. Hence, enhancing the low dynamic range discriminative features of HDR data could provide an effective route for better expression representation. Also, considering that entropy is a natural tool to characterize the ability of exhibiting the richness of image content, maximizing the entropy of the expression data is a reasonable approach to enhance weak discriminative features. Following this observation, we propose a novel coarse-to-fine Depth Distortion Constraint based Globally Optimal Entropy Maximization (GEMax) technique to pursue the maximal amount of information from the discriminative dynamic range for FER with multi-scale feature representation.

Method. The proposed GEMax contains three stages: S1) Range Selection, S2) Depth Distortion Constraint based Globally Optimal Entropy Maximization and S3) Data Collection. In stage S1, we examine the full dynamic range to preserve critical features in D_{dis} with discriminative range r_{dis} , and eliminate the expression-irrelative data at a coarse level. Then in stage S2, entropy of D_{dis} is maximized to represent the optimal information at a fine level. To overcome the face deformation caused by over-enhancement in unconstrained tone mapping, we introduce a depth distortion constraint τ , and significantly reduce the complexity from $O(KN^2)$ to $O(KN\tau)$ as well. We model the constrained optimization problem as finding a K -edges maximum weight path in a directed acyclic graph (DAG), and obtain the optimal solution with efficient dynamic programming. Finally, in stage S3, generated maps with different τ are collected together to jointly represent the facial expression and train the network. Here, we also design an effective Facial Attention (FA) structure with FA loss \mathcal{L}_{FA} to automatically locate discriminative facial parts for multi-scale feature learning. FA can be trained without extra facial landmark annotations.

Original contributions are summarized as follows.

- We demonstrate the effectiveness of enhancing raw point clouds for FER from the viewpoint of information theory. To the best of our knowledge, this is the first work using non-geometrical strategy for map generation in deep learning based 2D+3D FER methods.

- We propose a novel map generation technique GEMax for 2D+3D FER by maximizing the globally optimal entropy of the discriminative dynamic range with a new depth-distortion constraint.
- We design an efficient Facial Attention (FA) structure to automatically locate local facial parts for multi-scale learning. FA can be trained with facial attention loss \mathcal{L}_{FA} without any facial landmarks supervision.

Extensive experimental results show that our method significantly improves the entropy of the generated 3D maps from geometrical based methods: from 7.47 [35, 29] to 7.94. The proposed technique also outperforms state-of-the-art approaches in different 2D+3D FER benchmarks: BU-3DFE (89.72% vs. 88.35% [35]) and Bosphorus (83.63% vs. 82.50% [29]). Finally, ablation studies reveal the effectiveness of each step in the proposed method.

2. Related Works

FER methods can be divided into 2D FER, 3D FER and 2D+3D FER from the aspect of data modality. In this paper, we focus on 3D/2D+3D FER techniques, in which depth features are enhanced and represented by *Map Generation*.

2.1. Facial Expression Recognition (FER)

3D FER. The earlier literature adopts a variety of hand-crafted features for 3D FER tasks, such as Scale-Invariant Feature Transform (SIFT) in [1, 2], and Histogram Of Gradient (HOG) in [13, 14]. Recently, deep learning based methods learn 3D features by designing end-to-end Convolutional Neural Networks (CNN) with the following pipeline: 1) map generation; 2) feature extraction; 3) feature fusion; and 4) expression recognition. Li *et al.* [15] first converts depth data to five geometric maps, then adopts a pre-trained VGG-19 [23] followed by linear SVMs, achieving accuracy level of 84.87% on BU-3DFE [18]. Yang *et al.* [30] generates facial attribute masks from landmarks to supervise the training of CNN model and achieves 75.90% on BU-4DFE [32]. More recently, Zhu *et al.* [35] proposes a Discriminative Attention-based CNN (DA-CNN) method with an accuracy level of 87.69%, in which salient regions are estimated by CNN to enhance the local facial features. Different from [35], Chen *et al.* [3] enhances facial 3D surface by proposing a novel human vision inspired pooling structure via Fast and Light Manifold CNN (FLM-CNN) to recognize expressions directly from point-cloud data. However, merely launching FER from 3D data is still insufficient due to the lack of rich texture information.

2D+3D FER. By utilizing both texture and depth scans for comprehensively inter-class difference representation, multi-modality FER techniques achieve higher gains than single-modality FER. Fu *et al.* [5] proposes a low-rank tensor completion (FERLrTC) to capture multi-linear low-rank

structure and achieves 82.89% on BU-3DFE. Li *et al.* [16] proposes a Deep Fusion CNN (DF-CNN) to combine feature learning and fusion via a unified end-to-end framework. It is the first work that introduces deep CNN and feature-level fusion to 2D+3D FER. Then, DA-CNN from Zhu *et al.* [35] is also designed to implicitly learn the salient multi-modality facial maps and it achieves 88.35% on BU-3DFE. Instead of learning full image features, Jan *et al.* [9] estimates 4 local facial parts from both 2D and 3D data with facial landmarks for feature fusion, achieving an impressive accuracy of 88.54% on BU-3DFE.

Different from the aforementioned methods, we solve 2D+3D FER task by enhancing the slight inter-class variations for 3D point clouds, and jointly learn the local-global multi-scale features via the Facial Attention structure.

2.2. Map Generation

Map Generation is critical in 3D and 2D+3D FER by representing raw depth scans with a series of 2D attribute maps in order to: 1) enhance discriminative depth features; and 2) generate uniform grids for network input.

Uniform quantization is the most straightforward way to generate low dynamic range images as adopted in [25, 7, 21, 9, 28]. It is simple and fast, but may cause potential information loss for small expression variations. Hence, Vieriu *et al.* [27] projects 3D data onto a cylindrical 2D plane for wide-range rotational invariance. Normal patterns and curvature components are used to describe the first order and second order local structure in [12] and [11, 34]. Li *et al.* [14, 13] also adopts shape index maps for surface representation. In recent years, multi-view strategy is widely used to fully exploit the geometry properties via local plane/cubic fitting methods [8, 6] for deep learning based FER, such as [16, 30, 9, 3, 29, 35]. For example, curvature maps, range images and facial masks are concatenated to form 3-channel data to augment expressions in [30]. Along this direction, Li *et al.* [15] introduces a novel map generation by using 5 different attribute maps, namely a geometry map, 3 normal maps and a normalized curvature map for joint feature learning. Similar techniques are also adopted in [29, 35].

Instead of exploring multi-view geometrical attributes, we construct a more effective map generation process from the viewpoint of information theory. Specifically, we propose to maximize the entropy of the discriminative dynamic range while restricting the large depth distortion.

3. Method

In the proposed method, raw HDR depth scans D are comprehensively represented by a series of LDR depth images via three stages: S1) Range Selection, S2) Depth Distortion Constraint based Globally Optimal Entropy Maximization and S3) Data Collection. After stages S1 and S2, diverse maps under different depth constraints are collected

in the S3 stage. Once accomplished, multi-scale feature learning via Facial Attention structure is employed in the final recognition stage.

3.1. Range Selection (S1)

We design Range Selection to extract the discriminative range r_{dis} from raw 3D data to preserve critical features while eliminating expression-irrelevant structures. Considering $r_{dis} = d_{dis}/r_z$, computing r_{dis} equates to finding the discriminative depth d_{dis} under fixed-depth resolution r_z . An intuitive direction is to decompose the raw point clouds D into a series of depth block $\{D_i\}$ with different depth, then evaluate each D_i independently to examine its contribution to the FER task. We search the raw data from depth d_{min} cm to d_{max} cm, starting from the nose as illustrated in Fig. 2, and generate overlapped depth blocks with incremental Δd . Here, d_{min} is the lower bound to keep the basic face structure and d_{max} is the maximum sampled depth.

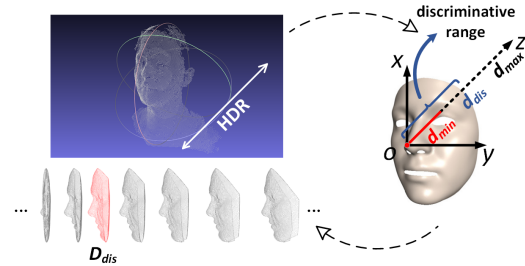


Figure 2. Illustration of Range Selection.

By evaluating D_i , we discover that point clouds data from different dynamic ranges contribute significantly unevenly to FER task. The recognition gap between the best depth block D_{dis} (with $d_i = 6$ cm) and the worst ($d_i = 14$ cm) is higher than 2.5% which is a huge gain in the current 2D+3D FER task. This observation reflects that the most discriminative expression features are located on limited shallow depth with limited dynamic range r_{dis} , and motivates us to further enhance the discriminative features for r_{dis} on a finer level.

3.2. Depth Distortion Constraint based Globally Optimal Entropy Maximization (S2)

The S2 stage takes the HDR depth block D_{dis} from the S1 stage as input, and produces LDR depth images I_d with enhanced features. Let N , K , and $K < N$ denote the number of the input and output depth levels, then mapping function from D_{dis} to I_d can be defined by an ordered integer vector

$$\mathbf{F} = \{d_0, d_1, \dots, d_k, \dots, d_K\}, \quad (1)$$

where $d_0 = 0$ and $d_K = N - 1$. In \mathbf{F} , any input depth data from range $[d_k, d_{k+1})$ will be mapped to the low dynamic

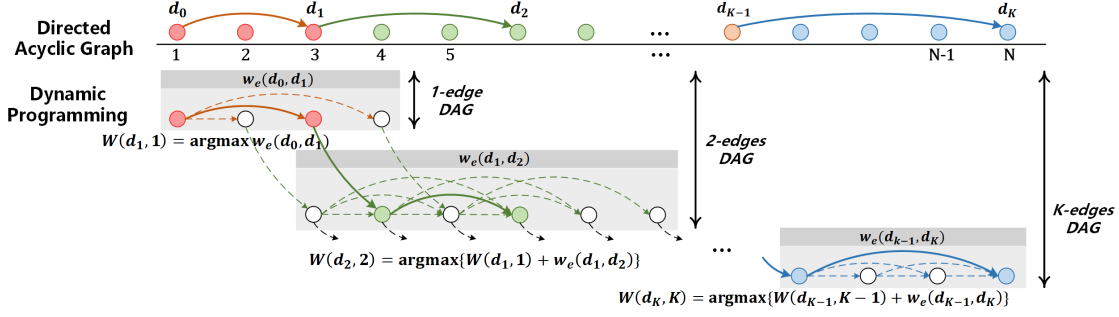


Figure 3. Dynamic programming process for solving K -edges maximum weight path optimization in DAG with depth distortion constraint.

intensity level k . With this setting, the objective function can be written as maximizing the entropy of I_d from D_{dis} with the mapping function \mathbf{F} as

$$\sum_k -P[d_k, d_{k+1}] \log P[d_k, d_{k+1}], \quad (2)$$

where $P[d_k, d_{k+1}] = \sum_{i=d_k}^{d_{k+1}} p_i$ is the probability of intensity k in LDR I_d . This can be calculated by accumulating p_i from $i = d_k$ to d_{k+1} in HDR depth data D_{dis} .

To solve this optimization problem, Histogram Equalization (HE) based methods with a global optimal solution seem to yield reasonable solutions. However, HE may over-enhance the depth image I_d by merging too many point clouds from D_{dis} with low probabilities. This will cause severe geometrical deformation and disrupt the face structure. Therefore, we introduce a depth distortion constraint condition rather entropy alone for map generation.

Depth Distortion Constraint. We define the depth distortion for each compressed bins k as

$$\varepsilon_k = (d_{k+1} - d_k)/N, \quad (3)$$

where $(d_{k+1} - d_k)$ denotes the number of bins in D_{dis} that would be mapped to k in I_d , and N is the dynamic range of D_{dis} for normalization. Considering that any bins of D_{dis} between range $[d_k, d_{k+1})$ would be mapped into one single depth value in the output depth image I_d , ε_k is a natural metric to evaluate the distortion loss of the mapping process. In this work, we constrain the maximal value of ε_k by enforcing $\varepsilon_k < \tau$ for any k in entropy maximization. Hence, the following additional constraint should be considered in the objective function:

$$1 \leq d_{k+1} - d_k \leq \tau, \text{ for any } k. \quad (4)$$

Finally, the objective of the S2 stage can be formulated as the following constrained optimization problem:

$$\begin{aligned} \mathbf{F} = \operatorname{argmax}_{\mathbf{F}} & \sum_{k=0}^{K-1} -P[d_k, d_{k+1}] \log P[d_k, d_{k+1}] \\ \text{s.t.} & \begin{cases} 0 \leq k \leq K-1, \\ 0 \leq d_k \leq N-1, \\ 1 \leq d_{k+1} - d_k \leq \tau, \text{ for any } k. \end{cases} \end{aligned} \quad (5)$$

It should be noticed that the value of depth distortion constraint τ should be in the range of $[N/K, N]$. If $\tau = N/K$, the map generation process becomes uniform quantization from N to K , known as range image. And if $\tau = N$, the new constraint will contribute nothing to the solution.

3.3. Graph Model and Dynamic Programming

To solve the constrained optimization in (5), an intuitive way is to greedy search the cumulative function such as HE, but this restricts the maximum searching length for every step to τ . However, the greedy strategy is NP hard (combinatorial) and might fall into locally optimal solutions. In pursuit of the globally optimal solution, we re-examine the constrained problem via graph theory, and propose a dynamic programming based solution.

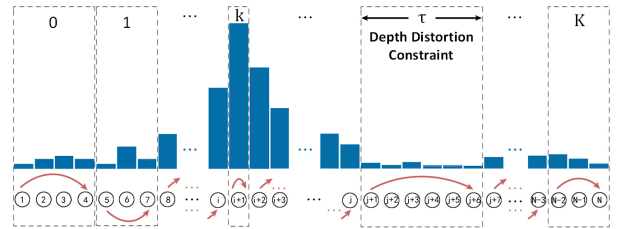


Figure 4. Illustration of graph theoretical based representation of the proposed map generation.

Graph model. First, let us define the graph model, where the input histogram of D_{dis} can be modeled by a directed acyclic graph (DAG) denoted by $G(V, E)$. The nodes of the DAG vertex set $V = \{1, 2, \dots, N\}$ represent the input depth levels d_k , and the path between any two nodes $[i, j)$ with $0 \leq i < j \leq N$ indicates the edge $e(i, j) \in E$. The weight of the edge $e(i, j)$ denoted by $w_e(i, j)$ represents the cost of mapping a depth range $[i, j)$ from D_{dis} to a single pixel in I_d as $w_e(i, j) = -P[i, j] \log P[i, j]$. With this set-up, the mapping function \mathbf{F} in (1) corresponds to a K -edges path in $G(V, E)$ linking node 0 to N , and the objective function in (5) is equivalent to seeking the optimal K -edges path in $G(V, E)$ with maximum weights $w_e(i, j)$ under the depth distortion constraint from (4). Considering

that the depth distortion is defined by the maximum number of the combined bins in the mapping function \mathbf{F} , the constraint (4) can be satisfied by not allowing any edge from node i to j if $j - i > \tau$ in the construction of $G(V, E)$ as illustrated in Fig. 4. In this fashion, the constrained optimization problem (5) can be rewritten as the following unconstrained equivalence:

$$W(N, K) = \operatorname{argmax}_{\mathbf{F}} \sum_{k=0}^{K-1} w_e(d_k, d_{k+1}) \quad (6)$$

where $W(N, K)$ is any path in $G(V, E)$ starting from the node 0 and ending at node N with K edges determined by \mathbf{F} .

However, solving the unconstrained optimization problem in (6) is still NP-hard since we have to emulate all possible paths in $G(V, E)$. Therefore, we investigate an efficient dynamic programming solution for (6), which can be performed in polynomial time.

Dynamic programming solution. Considering that if $d_0 \rightarrow d_K$ is the K -edges maximum weight path from vertex 0 to N , then the subpath $d_0 \rightarrow d_{K-1}$ must be the $(K-1)$ -edges maximum weight path from 0 to d_{K-1} . With this divide-and-conquer strategy, the original optimization problem of $W(N, K)$ in (6) can be represented by a series of sub-problems as shown in the following recursive form:

$$\begin{aligned} W(N, K) &= \operatorname{argmax}_{\mathbf{F}} \sum_{k=0}^{K-2} w_e(d_k, d_{k+1}) + w_e(d_{K-1}, d_K) \\ &= \operatorname{argmax}_{d_{K-1}} (W(d_{K-1}, K-1) + w_e(d_{K-1}, d_K)) \\ &= \dots \\ &= \operatorname{argmax}_{d_1} (W(d_1, 1) + \sum_{k=1}^{K-1} w_e(d_k, d_{k+1})). \end{aligned} \quad (7)$$

To iteratively solve (7), we first solve the 1-edge maximum weight path problem $W(x, 1)$ subject to $0 < x < \tau$, which is exactly the weight of edge $e(0, x)$, as the beginning step of dynamic programming. Then, in the next iteration, we focus on the 2-edge maximum weight path task $W(x, 2)$ and obtain the optimal solution by traversing all the possible intermediate vertices v via

$$W(x, 2) = \operatorname{argmax}_v (W(v, 1) + w_e(v, x)). \quad (8)$$

Similarly, 3-to- K -edges maximum weight path problems $W(x, 3)$ to $W(x, K)$ can be solved consequently by repeating (8) multiple times until we exhaust the maximum weight path $W(N, K)$ as Fig. 3 illustrates.

Complexity analysis. The dynamic programming process can be regarded as filling a table with $K \times N$ cells. The computation of any cell $W(X, Y)$ needs to traverse all possible intermediate vertices from 1 to $X - 1$. Hence, the

overall complexity of solving $W(N, K)$ is $O(KN^2)$. But in the proposed method, the maximum length of edge in graph $G(V, E)$ is bounded by the depth constraint τ . Therefore, only τ vertices from $X - \tau$ to $X - 1$ need to be traversed, reducing the complexity from $O(KN^2)$ to $O(KN\tau)$.

3.4. Facial Attention for Multi-Scale Learning

To further extract subtle local features, we design an additional Facial Attention module to automatically locate the discriminative facial parts in multi-scale learning without requiring any extra landmarks. This FA structure is depicted in Fig. 5.

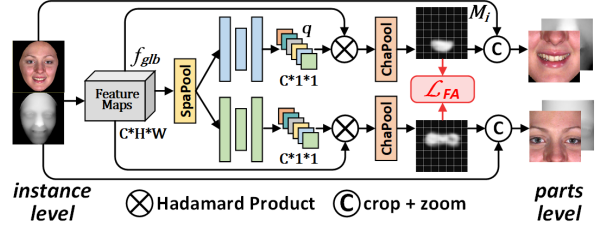


Figure 5. Structure of Facial Attention.

In the FA structure, global features f_{glb} with size $C * H * W$ from texture image I_t or generated 3D maps I_d are extracted by a series of convolutional layers. Then, a spatial average pooling (SpaPool) layer followed by a fully-connected based auto-encoder structure is constructed to project the feature map f_{glb} to a query vector q with size $C * 1 * 1$. In the query vector, we force the value from q to indicate the importance of the corresponding channel in f_{glb} . Hence, we can repeat q cross spacial domain, and implement the Hadamard product to re-weight the original global feature f_{glb} , and then average the feature intensities of the result for the same receptive field via a channel average pooling (ChaPool) layer to obtain the facial attention map $M = \{M_i\}, i = 1, \dots, N_M$.

To train the FA network, auxiliary classifiers are constructed after the ChaPool layer as the only supervision step without any extra parts annotations. Unfortunately, only class-wise labels are not enough due to the two channels in FA may fall into the same local minima, resulting in the non-distinctive facial parts between M_i . Hence, we design the following Facial Attention loss \mathcal{L}_{FA} to constrain: 1) the diversity of the discriminative parts; and 2) the concentration of each M_i as follows.

$$\begin{aligned} \mathcal{L}_{FA} &= \sum_{i=1}^{N_M} \sum_{(x,y)} \alpha M_i(x, y) \cdot (\max_{j \neq i} M_j(x, y) - \operatorname{mrg}) + \\ &\quad \beta M_i(x, y) \cdot (||x - t_x||^2 + ||y - t_y||^2). \end{aligned} \quad (9)$$

In this loss function, the first term evaluates the diversity

between any two attention map M_i whereas the second term measures the local distribution around peak magnitude (t_x, t_y) for each M_i . The two terms are balanced by parameters α and β , and avg makes \mathcal{L}_{FA} robust to noise. Next, the total loss \mathcal{L} is then the sum of cross entropy loss and FA loss and can be expressed as $\mathcal{L} = \lambda_{CE}\mathcal{L}_{CE} + \lambda_{LA}\mathcal{L}_{LA}$.

The FA module can be embedded in any existing 2D+3D FER CNNs. In our method, we construct the framework by integrating the proposed GEMax and FA module for multi-scale learning. More specifically, enhanced depth maps are firstly generated by GEMax, then the FA module is used to automatically predict the local facial parts. Both full images and generated parts are jointly learned by VGG-16, and finally all features are fused and then fed into the classifier for the final prediction. More structure details are illustrated in the Supplementary Materials.

4. Experiments

4.1. Dataset and Experiment Protocol

BU-3DFE [18] (Binghamton University 3D Facial Expression) benchmark includes 100 subjects for 2D+3D static FER. Each subject has six basic expressions (i.e. Angry, Disgust, Fear, Happy, Sad and Surprise) with four mild-to-strong intensity levels and one neutral expression, resulting a total $100 \times (4 \times 6 + 1) = 2500$ texture-depth data pairs. We follow the common protocol used in [13, 16, 17, 9, 3, 35] and use the highest 2 intensity levels for training and testing. In training, a partition of 60 subjects is randomly selected out of 100 people, repeating 100 rounds independently. In each round, 54 subjects (with $54 \times 2 \times 6 = 648$ pairs) are used for training and validation, and the remaining 6 (72 pairs) are for testing. 10-fold cross validation is utilized in each round for more stable performances.

Bosphorus [22] is a relatively small but more challenging face database for multi-modality FER tasks. It contains a total 4,666 2D texture and 3D depth image pairs from 105 subjects under adverse conditions, such as diverse poses and occlusions. But only 65 people contain all six prototype expressions. Followed by a common protocol as that of [16, 29, 28, 5], 60 samples are randomly selected from 65 subjects. Similarly to BU-3DFE, we repeat each round 100 times for comprehensively stable accuracy, and design a 10-fold cross validation for each round. Specifically, in each round, 90% data ($60 \times 0.9 \times 6 = 324$ image pairs) are used for training and validation, and the remaining 10% samples are reserved for testing.

4.2. Implementation Details

Network structure. To be consistent with previous methods [16, 35, 9], we employ VGG-16 [23] as the backbone. For FA module, the number of attention map N_M

is set to 2, which means two different facial parts will be generated for each sample. The auto-encoder structure is designed with 512-64-512 FC layers followed by ReLU activations. Global feature map f_{glb} is extracted from the last convolutional layer of VGG-16 with size [512, 7, 7], and the size of attention map M_i is 7×7 . Discriminative facial parts from the FA module are cropped from the input texture and depth data to size 96×96 , and then upsampled to the fixed size 224×224 . After the FA module, all the generated discriminative facial parts as well as full images are fed into VGG-16 for joint feature extraction, and then be fused to a single feature map with size $[6 \times 512, 7, 7]$ for final expression classification.

Training. All input 2D-3D pairs are resized to 224×224 . We train the network from scratch with batch size 32, and adopt the Adam optimizer with momentum [0.9, 0.999] and weight decay 0.001 for 30 epochs optimization. Learning rate is initialized to 0.1, and decreased by a factor of 10 every 10 epochs. For the loss function, we set $\lambda_{CE} = 1.0$, $\lambda_{LA} = 1.0$, and $\alpha = 1e3$ and $\beta = 1e2$ in (9). For GEMax, the depth range d_i is selected as 6 cm for the stage of S2, and the depth distortion constraint τ is set to $\tau = 20, 30, 40, 50, 60$ for training and $\tau = 20$ for testing.

4.3. Accuracy Comparison

3D and 2D+3D FER methods with and without extra facial landmark annotations are compared in Tab. 1 and Tab. 2 for BU3DFE and Bosphorus, respectively. In these tables, 'Map' means the map generation process, and the entropy of the generated maps is evaluated in the column labeled 'Entropy'. 'Feat.' and 'Acc.' stand for model feature and accuracy. The accuracy levels in the brackets indicate that the model is trained with additional annotations, such as facial landmarks from Facial Action units (FACs) system. To have a comprehensive comparison, we also provide an additional variant model denoted by (-GeM), which is trained using geometry maps.

For BU-3DFE dataset as shown in Tab. 1, our method achieves the best 89.72% accuracy for 2D+3D FER, surpassing the SOTA CNN based method [35] 1.37%. Though [9] achieves slightly better performance than [35], it uses 49 facial landmarks for training as the additional supervision for 2D-3D feature locating. Almost all of the CNN methods [16, 3, 29, 35] use geometry maps (GeM) for map generation, but the entropy of GeM (7.47) is lower than the proposed GEMax (7.94), indicating a lower amount of represented information. For traditional methods, diverse maps are used to describe the feature of depth in both 3D and 2D+3D tasks, including Range Image (RI), Curvature Maps (CuM), Normal Maps (NoM) and Conformal Factor Images (CFI), but the performances are lower than CNN models and our method.

Similar results from Bosphorus benchmark can be found

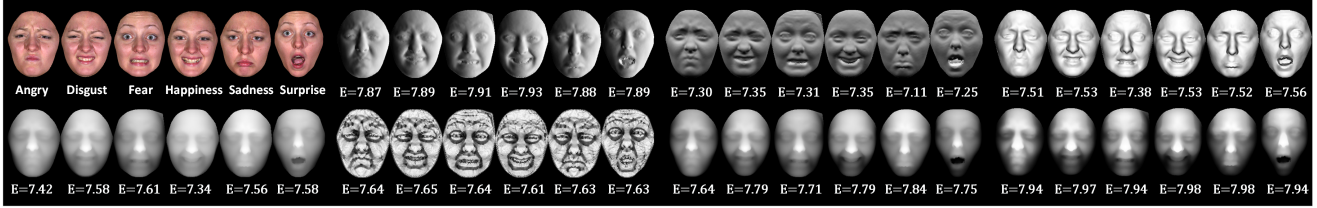


Figure 6. Map generation comparisons. First row from left to right: RGB images, Normal Maps on x-axis, y-axis and z-axis. Second row: Range Images, Curvature Maps, GEMax (S1), GEMax (S2). Our method achieves the highest entropy (E) with complete facial structure.

Table 1. FER comparisons on BU-3DFE dataset.

Method	Domain	Map	Feat.	Entropy	Acc.(%)
Gong <i>et al.</i> [7]	3D	RI	BFSC	7.21	(76.22)
Berretti <i>et al.</i> [2]	3D	RI	SIFT	7.21	(77.54)
Zeng <i>et al.</i> [33]	3D	CFI	SC	-	70.93
Li <i>et al.</i> [12]	3D	NoM	LNP	7.57	80.14
Li <i>et al.</i> [14]	3D	CuM	HOG	7.63	(82.01)
Lemaire <i>et al.</i> [11]	3D	CuM	HOG	7.63	76.61
Zhen <i>et al.</i> [34]	3D	CuM	HOG	7.63	83.20
Yang <i>et al.</i> [31]	3D	GeM	SIFT	7.47	84.80
Chen <i>et al.</i> [3]	3D	GeM	CNN	7.47	(86.67)
Zhu <i>et al.</i> [35]	3D	GeM	CNN	7.47	87.69
Fu <i>et al.</i> [5]	2D+3D	GeM	LBP	7.47	82.89
Li <i>et al.</i> [13]	2D+3D	CuM	HOG	7.63	(86.32)
Jan <i>et al.</i> [9]	2D+3D	RI	LBP	7.21	(86.89)
Li <i>et al.</i> [16]	2D+3D	GeM	CNN	7.47	86.86
Wei <i>et al.</i> [29]	2D+3D	GeM	CNN	7.47	88.03
Zhu <i>et al.</i> [35]	2D+3D	GeM	CNN	7.47	88.35
Jan <i>et al.</i> [9]	2D+3D	RI	CNN	7.21	(88.54)
ours(-GeM)	2D+3D	GeM	CNN	7.47	89.11
ours	2D+3D	GEMax	CNN	7.94	89.72

in Tab. 2, where our method again consistently achieves SOTA accuracies 83.05% and 83.63% with geometry maps and GEMax, surpassing all CNN and hand-crafted based competitors.

Table 2. FER comparisons on Bosphorus dataset.

Method	Domain	Map	Feat.	Entropy	Acc.(%)
Li <i>et al.</i> [12]	3D	NoM	LNP	7.52	75.83
Yang <i>et al.</i> [31]	3D	NoM	SIFT	7.52	77.50
Fu <i>et al.</i> [5]	2D+3D	GeM	LBP	7.48	75.93
Li <i>et al.</i> [13]	2D+3D	SIM	HOG	7.65	(79.72)
Tian <i>et al.</i> [26]	2D+3D	NoM	CNN	7.52	79.17
Li <i>et al.</i> [16]	2D+3D	GeM	CNN	7.48	80.00
Li <i>et al.</i> [16]	2D+3D	GeM	CNN	7.48	80.28
Wei <i>et al.</i> [29]	2D+3D	GeM	CNN	7.48	82.22
Vo <i>et al.</i> [28]	2D+3D	RI	CNN	7.13	82.40
Wei <i>et al.</i> [29]	2D+3D	GeM	CNN	7.48	82.50
ours(-GeM)	2D+3D	GeM	CNN	7.48	83.05
ours	2D+3D	GEMax	CNN	7.92	83.63

4.4. Entropy Evaluation

GEMax significantly improves the entropy of depth data from Range Image (RI) 7.21 \rightarrow 7.94 and 7.13 \rightarrow 7.92 for BU-3DFE and Bosphorus in Tab. 1 and Tab. 2 (column labeled 'Entropy'). Widely used Geometrical Maps (GeM) have the average entropy of 7.47 by combining RI, NoM and CuM. Expression-level entropy for map generation are illustrated in Fig. 6, in which our method achieves the highest expression entropy with complete face information.

4.5. Running Time

Since there is no parallel operation, GEMax can be easily launched on CPU machine without GPUs. Here, we use a single Intel Core i5-8250U CPU. Notice that map generation can be performed before network training and testing, and GEMax will not affect the inference time of CNN.

Table 3. Time-Entropy evaluation of GEMax.

τ	16	20	30	40	50	60	N
time (s)	0.21	0.22	0.23	0.25	0.29	0.30	33.9
FPS	4.67	4.44	4.24	3.89	3.44	3.29	0.029
Entropy	7.606	7.811	7.931	7.964	7.980	7.987	7.993

Tab. 3 evaluates the running time on BU-3DFE dataset with image size 224×224 . GEMax takes an average of 0.22s per image when $\tau = 20$, and increases about 0.016s for every interval $\Delta\tau = 10$. As a comparison, the time of using full depth range search without τ (or $\tau = N$) is an unacceptable 33.9s per image with very little entropy gains (7.993 vs. 7.987), which validates the high efficiency of introducing the depth distortion constraint τ .

4.6. Limitation

Although satisfying results are achieved, semantic information is not considered in the proposed map generation. This may cause the negative enhancement of some facial parts that give more information about the entire face, but contribute less to the discriminative expression feature. For example, Fear is often misclassified as Disgust with a False Negative (FN) rate of 14.31% because chasing the maximal entropy of the full image (eyes + mouth) not only enhancing the discriminative regions (eyes) but also augmenting the relatively confusing parts (mouth).

5. Ablation Study

Depth range section. The effectiveness of the diverse depth range from $d_{min} = 5$ cm to $d_{max} = 14$ are evaluated in Tab. 4. Here, 5 cm is the minimum depth to maintain the basic face structure and 14 cm is the maximum depth provided by the dataset. Data with larger d_i have more dynamic range.

Table 4. Ablation study of depth range selection d_i .

Dataset	Depth Range d_i / Acc.				
	5 cm	6 cm	7 cm	8 cm	9 cm
BU-3DFE	84.53%	84.92%	84.37%	83.79%	83.64%
	10 cm	11 cm	12 cm	13 cm	14 cm
	83.13%	82.77%	82.67%	82.62%	82.40%
Bosphorus	5 cm	6 cm	7 cm	8 cm	9 cm
	79.31%	79.47%	79.13%	78.92%	78.64%
	10 cm	11 cm	12 cm	13 cm	14 cm
	78.64%	78.39%	78.22%	78.17%	78.10%

In the table, best results are achieved at $d_i = 6$ cm for both datasets, indicating that facial structure within 6 cm depth contains the most distinctive information for expressions. Depth range larger than 6 cm will introduce redundant and expression-irrelevant information, and gradually decreases the recognition rate.

Depth distortion constraint. Raw point clouds are first uniformly quantified from 32-bit to 16-bit to avoid the infeasible 2^{32} bins histogram calculating. Then, we evaluate the model under different constraints with τ ranging from 16 to 60.

Table 5. Ablations of depth distortion constraint τ .

Dataset	BU-3DFE					
τ	16	20	30	40	50	60
Acc.	84.92%	85.81%	85.74%	85.33%	85.26%	85.25%
Entropy	7.61	7.81	7.93	7.96	7.98	7.99
Dataset	Bosphorus					
τ	16	20	30	40	50	60
Acc.	79.47%	80.12%	80.09%	79.83%	79.64%	79.64%
Entropy	7.55	7.77	7.91	7.95	7.97	7.98

In Tab. 5, lower τ value means stronger constraint. Hence, $\tau = 16$ indicates the uniform mapping from $N = 2^{16} = 4096$ to $K = 256$ bins with minimal entropy. Larger τ relaxes the constraint and produces more entropy gain, but it may also over-enhance the image by chasing the maximal output entropy as shown in Fig. 7, where the contrast of local regions such as the nose and the forehead are often over promoted, leading to geometric deformations.

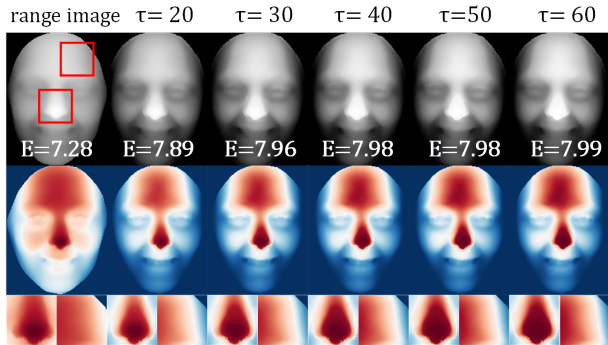


Figure 7. Ablation study of depth distortion constraint τ . Left column: range image. Right columns: GEMax with different τ . Larger τ achieves higher entropy (E) with loose constraint, but may cause the over enhancement of local facial parts.

Table 6. Evaluation of multi-scale learning. Facial parts generated from the proposed FA module are discriminative, and multi-scale learning with local-global images achieves the best performances.

Dataset	Input	Texture	Depth	Both
BU-3DFE	Full image	86.79%	86.87%	89.72%
	Facial part	76.39%	75.43%	
Bosphorus	Full image	79.64%	81.42%	83.63%
	Facial part	68.17%	73.21%	

Multi scale learning. Multi-scale inputs including full images and facial parts from the FA module are tested in Tab. 6. Facial parts from the FA module only describe a local neighbor structure of the entire face, but recognizing rate from facial parts without complete face information can still achieve a satisfying accuracy (within 10% drop), demonstrating the effectiveness of FA module. By jointly considering both full images and facial parts, the overall performance using multi-scale learning can be further boosted.

6. Conclusion

In this paper, we have proposed a novel map generation method and a Facial Attention structure for 2D+3D FER task. Taking full advantage of the two improvements, slight expression variations from the discriminative dynamic range are comprehensively enhanced by maximizing the entropy under the depth distortion constraint, and local facial parts can be efficiently generated for multi-scale feature learning. Extensive experiments on different datasets produce state-of-the-art results, demonstrating the generalization ability and the effectiveness of our proposed model. In the future, we will extend the approach to enhance more challenging HDR data, such as infra-red or SAR images, and generalize FA module to 4D (3D + video) FER by exploring the temporal face structure information.

References

- [1] Stefano Berretti, Boulbaba Ben Amor, Mohamed Daoudi, and Alberto Del Bimbo. 3d facial expression recognition using sift descriptors of automatically detected keypoints. *The Visual Computer*, 27:1021–1036, 11 2011. [2](#)
- [2] Stefano Berretti, Alberto Del Bimbo, Pietro Pala, Boulbaba Ben Amor, and Mohamed Daoudi. A set of selected sift features for 3d facial expression recognition. In *2010 20th International Conference on Pattern Recognition*, pages 4125–4128, Aug 2010. [2, 7](#)
- [3] Zhixing Chen, Di Huang, Yunhong Wang, and Liming Chen. Fast and light manifold cnn based 3d facial expression recognition across pose variations. *Proceedings of the 26th ACM international conference on Multimedia*, 2018. [1, 2, 3, 6, 7](#)
- [4] David DeVault, Ron Artstein, Grace Benn, Teresa Dey, Edward Fast, Alesia Gainer, Kallirroi Georgila, Jonathan Gratch, Arno Hartholt, Margot Lhommet, Gale M. Lucas, Stacy Marsella, Fabrizio Morbini, Angela Nazarian, Stefan Scherer, Giota Stratou, Apar Suri, David R. Traum, Rachel Wood, Yuyu Xu, Albert A. Rizzo, and Louis-Philippe Morency. Simsensei kiosk: a virtual human interviewer for healthcare decision support. In *AAMAS*, 2014. [1](#)
- [5] Yunfang Fu, Qiuqi Ruan, Ziyang Luo, Yi Jin, Gaoyun An, and Jun Wan. Ferlrc: 2d+3d facial expression recognition via low-rank tensor completion. *Signal Processing*, 161:74 – 88, 2019. [1, 2, 6, 7](#)
- [6] Jack Goldfeather and Victoria Interrante. A novel cubic-order algorithm for approximating principal direction vectors. *ACM Trans. Graph.*, 23(1):45–63, Jan. 2004. [2, 3](#)
- [7] Boqing Gong, Yueming Wang, Jianzhuang Liu, and Xiaoou Tang. Automatic facial expression recognition on a single 3d face by exploring shape deformation. In *Proceedings of the 17th ACM International Conference on Multimedia*, MM ’09, pages 569–572, New York, NY, USA, 2009. ACM. [3, 7](#)
- [8] Richard Hoffman and Anil K. Jain. Segmentation and classification of range images. *IEEE Transactions on Pattern Analysis and Machine Intelligence*, PAMI-9(5):608–620, 1987. [2, 3](#)
- [9] Asim Jan, Huaxiong Ding, Hongying Meng, Liming Chen, and Huibin Li. Accurate facial parts localization and deep learning for 3d facial expression recognition. In *2018 13th IEEE International Conference on Automatic Face Gesture Recognition (FG 2018)*, pages 466–472, May 2018. [3, 6, 7](#)
- [10] Ashish Kapoor, Winslow Burleson, and Rosalind W. Picard. Automatic prediction of frustration. *International Journal of Human-Computer Studies*, 65(8):724 – 736, 2007. [1](#)
- [11] Pierre Lemaire, Mohsen Ardabilian, Liming Chen, and Mohamed Daoudi. Fully automatic 3d facial expression recognition using differential mean curvature maps and histograms of oriented gradients. In *2013 10th IEEE International Conference and Workshops on Automatic Face and Gesture Recognition (FG)*, pages 1–7, April 2013. [3, 7](#)
- [12] Huibin Li, Liming Chen, Di Huang, Yunhong Wang, and Jean-Marie Morvan. 3d facial expression recognition via multiple kernel learning of multi-scale local normal patterns. In *Proceedings of the 21st International Conference on Pattern Recognition (ICPR2012)*, pages 2577–2580, Nov 2012. [3, 7](#)
- [13] Huibin Li, Huaxiong Ding, Di Huang, Yunhong Wang, Xi Zhao, Jean-Marie Morvan, and Liming Chen. An efficient multimodal 2d + 3d feature-based approach to automatic facial expression recognition. *Computer Vision and Image Understanding*, 140:83 – 92, 2015. [1, 2, 3, 6, 7](#)
- [14] Huibin Li, Jean-Marie Morvan, and Liming Chen. 3d facial expression recognition based on histograms of surface differential quantities. In Jacques Blanc-Talon, Richard Kleihorst, Wilfried Philips, Dan Popescu, and Paul Scheunders, editors, *Advanced Concepts for Intelligent Vision Systems*, pages 483–494, Berlin, Heidelberg, 2011. Springer Berlin Heidelberg. [2, 3, 7](#)
- [15] Huibin Li, Jian Sun, Dong Wang, Zongben Xu, and Liming Chen. Deep representation of facial geometric and photometric attributes for automatic 3d facial expression recognition. 11 2015. [2, 3](#)
- [16] Huibin Li, Jian Sun, Zongben Xu, and Liming Chen. Multimodal 2d+3d facial expression recognition with deep fusion convolutional neural network. *IEEE Transactions on Multimedia*, 19(12):2816–2831, Dec 2017. [1, 3, 6, 7](#)
- [17] Qian Li, Gaoyun An, and Qiuqi Ruan. 3d facial expression recognition using orthogonal tensor marginal fisher analysis on geometric maps. In *2017 International Conference on Wavelet Analysis and Pattern Recognition (ICWAPR)*, pages 65–71, July 2017. [6](#)
- [18] Lijun Yin, Xiaozhou Wei, Yi Sun, Jun Wang, and M. J. Rosato. A 3d facial expression database for facial behavior research. In *7th International Conference on Automatic Face and Gesture Recognition (FG 2006)*, pages 211–216, April 2006. [2, 6](#)
- [19] Paris Mavroumoustakos Blom, Sander Bakkes, Chek Tien Tan, Shimon Whiteson, Diederik Roijers, Roberto Valenti, and T. Gevers. Towards personalised gaming via facial expression recognition. 10 2014. [1](#)
- [20] Elnar Hajiyev Mihkel Jaatma, Martin Salo. Realeyes. <https://www.realeyesit.com/>. [1](#)
- [21] Oyebeade K. Oyedotun, Girum Demisse, Abd El Rahman Shabayek, Djamila Aouada, and Björn Ottersten. Facial expression recognition via joint deep learning of rgb-depth map latent representations. In *2017 IEEE International Conference on Computer Vision Workshops (ICCVW)*, pages 3161–3168, 2017. [3](#)
- [22] Arman Savran, Neşe Alyüz, Hamdi Dibeklioglu, Oya Çeliktutan, Berk Gökberk, Bülent Sankur, and Lale Akarun. Bosphorus database for 3d face analysis. In Ben Schouten, Niels Christian Juul, Andrzej Drygajlo, and Massimo Tistarelli, editors, *Biometrics and Identity Management*, pages 47–56, Berlin, Heidelberg, 2008. Springer Berlin Heidelberg. [6](#)
- [23] Karen Simonyan and Andrew Zisserman. Very deep convolutional networks for large-scale image recognition. *CoRR*, abs/1409.1556, 2014. [2, 6](#)
- [24] Chek Tien Tan, Daniel Rosser, Sander Bakkes, and Yusuf Pisan. A feasibility study in using facial expressions analysis to evaluate player experiences. *ACM International Conference Proceeding Series*, 07 2012. [1](#)

- [25] Hao Tang and Thomas S. Huang. 3d facial expression recognition based on automatically selected features. In *2008 IEEE Computer Society Conference on Computer Vision and Pattern Recognition Workshops*, pages 1–8, June 2008. 3
- [26] Kun Tian, Liaoyuan Zeng, Sean McGrath, Qian Yin, and Wenyi Wang. 3d facial expression recognition using deep feature fusion cnn. In *2019 30th Irish Signals and Systems Conference (ISSC)*, pages 1–6, 2019. 7
- [27] Radu-Laurențiu Vieriu, Sergey Tulyakov, Stanislau Semeoniuta, Enver Sangineto, and Nicu Sebe. Facial expression recognition under a wide range of head poses. In *2015 11th IEEE International Conference and Workshops on Automatic Face and Gesture Recognition (FG)*, volume 1, pages 1–7, 2015. 3
- [28] Quang Nhat Vo, Khanh Tran, and Guoying Zhao. 3d facial expression recognition based on multi-view and prior knowledge fusion. In *2019 IEEE 21st International Workshop on Multimedia Signal Processing (MMSP)*, pages 1–6, 2019. 3, 6, 7
- [29] Xiaofan Wei, Huibin Li, Jian Sun, and Liming Chen. Unsupervised domain adaptation with regularized optimal transport for multimodal 2d+3d facial expression recognition. In *2018 13th IEEE International Conference on Automatic Face Gesture Recognition (FG 2018)*, pages 31–37, May 2018. 1, 2, 3, 6, 7
- [30] Huiyuan Yang and Lijun Yin. Cnn based 3d facial expression recognition using masking and landmark features. In *2017 Seventh International Conference on Affective Computing and Intelligent Interaction (ACII)*, pages 556–560, 2017. 1, 2, 3
- [31] Xudong Yang, Di Huang, Yunhong Wang, and Liming Chen. Automatic 3d facial expression recognition using geometric scattering representation. In *2015 11th IEEE International Conference and Workshops on Automatic Face and Gesture Recognition (FG)*, volume 1, pages 1–6, May 2015. 1, 7
- [32] Lijun Yin, Xiaochen Chen, Yi Sun, Tony Worm, and Michael Reale. A high-resolution 3d dynamic facial expression database. In *2008 8th IEEE International Conference on Automatic Face Gesture Recognition*, pages 1–6, 2008. 2
- [33] Wei Zeng, Huibin Li, Liming Chen, Jean-Marie Morvan, and Xianfeng David Gu. An automatic 3d expression recognition framework based on sparse representation of conformal images. In *2013 10th IEEE International Conference and Workshops on Automatic Face and Gesture Recognition (FG)*, pages 1–8, April 2013. 7
- [34] Qingkai Zhen, Di Huang, Yunhong Wang, and Liming Chen. Muscular movement model-based automatic 3d/4d facial expression recognition. *IEEE Transactions on Multimedia*, 18(7):1438–1450, July 2016. 1, 3, 7
- [35] Kangkang Zhu, Zhengyin Du, Weixin Li, Di Huang, Yunhong Wang, and Liming Chen. Discriminative attention-based convolutional neural network for 3d facial expression recognition. In *2019 14th IEEE International Conference on Automatic Face Gesture Recognition (FG 2019)*, pages 1–8, May 2019. 1, 2, 3, 6, 7